Properties of microturbulence in toroidal plasmas with reversed magnetic shear

Wenjun Deng and Zhihong Lin[a)]
Department of Physics and Astronomy, University of California, Irvine, California 92697, USA

(Received 6 August 2009; accepted 15 September 2009; published online 8 October 2009)

Electrostatic drift wave turbulence in tokamak plasmas with reversed magnetic shear is studied using global gyrokinetic particle simulations. The linear eigenmode of the ion temperature gradient (ITG) instability exhibits a mode gap around the minimum safety factor ($q_{\min}$) region, particularly when $q_{\min}$ is an integer, due to the rarefaction of rational surfaces. The collisionless trapped electron mode (CTEM) instability is suppressed in the negative-shear region due to the reversal of the toroidal precessional drift of trapped electrons. However, after nonlinear saturation, the ITG gap is filled up by the turbulence spreading and the CTEM fluctuation propagates into the stable negative-shear region. The steady state turbulence occupies the whole volume without any identifiable gap or coherent structures of the heat conductivity, perturbed temperature, or zonal flows in the $q_{\min}$ location or the reversed shear region. Our finding indicates that the electrostatic drift wave turbulence itself does not support either linear or nonlinear mechanism for the formation of internal transport barriers in the reversed magnetic shear when $q_{\min}$ crossing an integer. © *2009 American Institute of Physics*. [doi:10.1063/1.3243918]

I. INTRODUCTION

Turbulent transport in toroidal plasmas is usually driven by microscopic drift wave instabilities,[1] of which the linear properties could be affected by the magnetic shear (radial derivative of the safety factor q). Tokamak experiments with reversed magnetic shear[2–4] observed improved confinement and formation of internal transport barriers. A minimum of the safety factor ($q_{\min}$) exists in these experiments roughly in the middle of the radial direction so that the magnetic shear is negative (reversed) in the core and positive (normal) at the edge.

Several mechanisms based on the linear theory of the electrostatic, toroidal drift wave eigenmodes have been proposed to explain the reduction of the turbulent transport in the reversed shear plasmas. A popular theory is that the zero magnetic shear at the radial location of the $q_{\min}$ weakens the coupling of the poloidal harmonics, which creates a gap in the toroidal eigenmodes of the ion temperature gradient (ITG) instability[5] around the $q_{\min}$ region due to the rarefaction of the mode rational surfaces[6] or the presence of a flow shear.[7] Beyond the linear theory, a gap in the fluctuation intensity could also be created by enhanced generation of sheared flows[6,8] and convective cells,[9] or the fluctuation-induced profile corrugations.[10] However, some nonlinear simulations do not observe such a mode gap due to the existence of a slablike branch of the ITG instability[11] or the turbulence spreading and avalanche.[12] Another possible mechanism is that the reversal of the magnetic shear can reverse the direction of the toroidal precessional drift of magnetically trapped electrons,[13] and therefore suppress the collisionless trapped electron mode (CTEM) driven by the precessional resonance.[14]

The width of the linear mode gap is larger if $q_{\min}$ is a lower order rational number, particularly an integer. Indeed, many tokamak experiments[15–18] observed the formation of internal transport barriers when the time-dependent $q_{\min}$ passing through an integer value. The onset of the transport barriers is sometimes accompanied by bursts of magnetohydrodynamic (MHD) activities.[19,17] The generation of sheared flows by the MHD modes has been conjectured to be able to suppress the transport driven by the electrostatic microturbulence.[20,21] However, the mechanism of the MHD-generated sheared flows has not been tested in a fully self-consistent nonlinear simulation treating both MHD modes and microturbulence. In short, the experimental evidence of the correlation between the formation of internal transport barriers and the $q_{\min}$ crossing an integer is not well understood.

In this work, we investigate the linear and nonlinear properties of the electrostatic toroidal drift wave turbulence in the reversed magnetic shear plasmas with the $q_{\min}$ being a low-order rational number, particularly an integer. Global simulations using the gyrokinetic toroidal code (GTC) (Ref. 22) of the electrostatic ITG turbulence shows that a large mode gap appears in the linear phase when $q_{\min}$ is an integer. The width of the gap increases when the curvature of the q-profile decreases. The gap is filled up after the nonlinear saturation by the turbulence spreading[23–25] from both core and edge. The flux of the fluctuation energy filling in the gap has been measured. In the steady state turbulence, there is no clear gap or coherent structures around the $q_{\min}$ region for the ion heat conductivity, temperature perturbation, or zonal flows. The simulations of the electrostatic CTEM turbulence show that the linear eigenmodes only appear in the normal shear region. After the nonlinear saturation, the turbulence spreads across the $q_{\min}$ surface into the reversed shear region. The turbulence spreading is characterized by a front propa-

[a)]Author to whom correspondence should be addressed. Electronic mail: zhihongl@uci.edu.

gation with a speed of about half of the electron diamagnetic flow. The steady state turbulence occupies the whole volume without any identifiable structure correlated with the $q_{\min}$ or the reversed shear region.

Our global gyrokinetic particle simulation results indicate that the electrostatic drift wave turbulence itself does not support either linear or nonlinear mechanism for the formation of internal transport barriers in the reversed magnetic shear when $q_{\min}$ crossing an integer. Other external mechanisms, such as sheared flows generated by MHD activities, are worth pursuing as possible agents to suppress the electrostatic drift wave turbulence and form the internal transport barriers when $q_{\min}$ crossing an integer. Our results of nonlocal effects also raise the issue of the validity of previous local simulations finding the transport reduction due to the drift reversal or the rarefaction of mode rational surfaces in the reversed shear plasmas.

The paper is organized as follows. The simulation model is described in Sec. II. The simulations of the ITG turbulence and the CTEM turbulence are discussed in Secs. III and IV, respectively. Section V summarizes the results and gives the conclusions.

II. SIMULATION MODEL

In electrostatic simulations, the plasma is described by the electrostatic gyrokinetic equation:[26,27]

$$\frac{d}{dt}f_\sigma(\boldsymbol{X},\mu,v_\parallel,t) \equiv \left[\frac{\partial}{\partial t}+\dot{\boldsymbol{X}}\cdot\nabla+\dot{v}_\parallel\frac{\partial}{\partial v_\parallel}\right]f_\sigma=0, \tag{1}$$

where $f_\sigma(\boldsymbol{X},\mu,v_\parallel,t)$ is the particle distribution function in terms of the gyrocenter $\boldsymbol{X}$, the magnetic moment μ, the parallel velocity $v_\parallel$, and time t:

$$\dot{\boldsymbol{X}}=v_\parallel\boldsymbol{b}_0+\boldsymbol{v}_E+\boldsymbol{v}_g+\boldsymbol{v}_c, \tag{2}$$

$$\dot{v}_\parallel=-\frac{1}{m_\sigma}\frac{\boldsymbol{B}_0^*}{B_0}\cdot(\mu\nabla B_0+Z_\sigma\nabla\bar{\phi}), \tag{3}$$

$$\boldsymbol{B}_0^*=\boldsymbol{B}_0+\frac{v_\parallel}{\Omega_\sigma}\boldsymbol{b}_0\times\nabla B_0. \tag{4}$$

Here the subscript $\sigma=i,e$ stands for particle species, Z_σ is the particle electric charge, and m_σ is the particle mass. $\boldsymbol{B}_0$ is the equilibrium $\boldsymbol{B}$-field and $\boldsymbol{b}_0\equiv\boldsymbol{B}_0/B_0$ is the unit vector. $\bar{\phi}$ is the gyrophase-averaged electrostatic potential. The $\boldsymbol{E}\times\boldsymbol{B}$ drift velocity $\boldsymbol{v}_E$, the ∇B drift velocity $\boldsymbol{v}_g$, and the curvature drift velocity $\boldsymbol{v}_c$ are given by:

$$\boldsymbol{v}_E=\frac{c\boldsymbol{b}_0\times\nabla\bar{\phi}}{B_0}, \tag{5}$$

$$\boldsymbol{v}_g=\frac{1}{m_\sigma\Omega_\sigma}\mu\boldsymbol{b}_0\times\nabla B_0, \tag{6}$$

$$\boldsymbol{v}_c=\frac{1}{\Omega_\sigma}v_\parallel^2\nabla\times\boldsymbol{b}_0. \tag{7}$$

The electrostatic potential ϕ is described by gyrokinetic Poisson's equation:[28]

$$\frac{1}{\lambda_{Di}^2}(\phi-\tilde{\phi})=4\pi\sum_\sigma Z_\sigma n_\sigma, \tag{8}$$

where $\lambda_{Di}^2\equiv T_i/(4\pi n_{0i}Z_i^2)$ is the ion Debye length, and $n_\sigma\equiv\int f_\sigma d\boldsymbol{v}$ is the particle density. $\tilde{\phi}$ is the second gyrophase-averaged potential and defined as[28,29]

$$\tilde{\phi}(\boldsymbol{x})=\frac{1}{2\pi}\int\bar{\phi}(\boldsymbol{X})f_{0i}(\boldsymbol{X},\mu,v_\parallel)\delta(\boldsymbol{X}-\boldsymbol{x}+\boldsymbol{\rho}_i)d\boldsymbol{X}d\mu dv_\parallel d\alpha, \tag{9}$$

where $f_{0i}(\boldsymbol{X},\mu,v_\parallel)$ is the ion equilibrium gyrocenter distribution function, $\boldsymbol{\rho}_i\equiv-\boldsymbol{v}_{i\perp}\times\boldsymbol{b}_0/\Omega_i$ is the ion gyroradius vector, Ω_i is the ion cyclotron frequency, and α is the gyrophase angle. In the long wavelength ($k_r\rho_i\ll1$) and high aspect ratio ($R_0/a\gg1$) limit, the zonal component of ϕ is described by

$$\frac{\rho_i^2}{\lambda_{Di}^2}\nabla_\perp^2\langle\phi\rangle=-4\pi\sum_\sigma Z_\sigma\langle n_\sigma\rangle, \tag{10}$$

where $\langle\cdot\rangle$ means averaging over the flux surface. The system described by Eqs. (1) and (8) is closed. In our simulations, GTC[30,31] uses the particle-in-cell method to solve the gyrocenter distribution functions and ϕ iteratively in the toroidal geometry. When solving Eq. (1), ions and electrons are treated differently because of their large mass ratio. For ions, field quantities on the guiding center are averaged over a gyro-orbit. Electrons are treated adiabatic in the simulations of the ITG turbulence. In the simulations of the CTEM turbulence, a fluid-kinetic hybrid electron model[32,33] based on the drift-kinetic limit of Eq. (1) is used.

The poloidal cross sections of the flux surfaces are concentric circles. Parabolic q-profiles with a reversed shear are used:

$$q(r)=q_{\min}+c_1(r/a-0.5)^2, \tag{11}$$

where a is the minor radius. The profile of $q(r)$ has a minimum value $q_{\min}$ at the $r=0.5a$ surface, which will be called the $q_{\min}$ surface in this paper. The value of c_1 represents the curvature of the q-profile. Temperature and density gradients have a profile of $\exp\{-[(r/a-0.5)/r_w]^6\}$. In this work hydrogen plasmas are simulated, which have the properties of $Z_i=+e$ and $m_i/m_e=1837$.

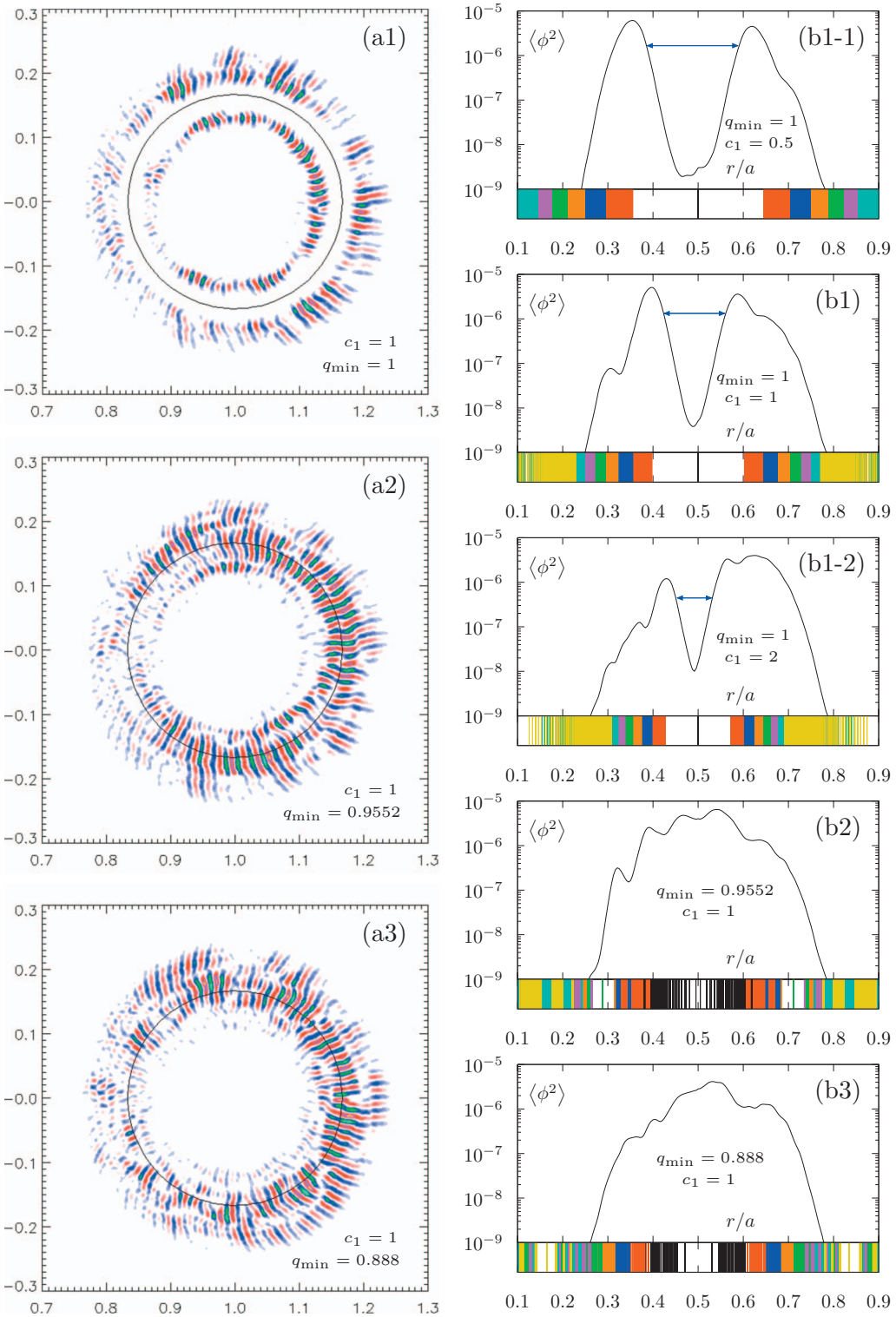

FIG. 1. (Color) The electrostatic potential ϕ structures of the ITG instability. Left column (a): ϕ in the poloidal plane, black circle indicating the $q_{\min}$ surface. Right column (b): flux-surface-averaged potential intensity $\langle\phi^2\rangle$ and rational surface distribution as a function of radius r.

III. ITG TURBULENCE

In toroidal plasmas, ion magnetic drift is faster in higher temperature regions and slower in lower temperature regions. When an electrostatic perturbation makes ripples on an isothermal surface, the difference in drift speed causes a charge accumulation, which then generates an electric field. In the outer region of the poloidal cross section, i.e., the so called bad curvature region, the $\boldsymbol{E}\times\boldsymbol{B}$ drift caused by such an electric field amplifies the ripples, therefore leading to an instability called the ITG instability.[1]

The ITG instability is excited when $\eta_i \equiv L_n/L_{T_i}$ is larger than a certain threshold value. The threshold value depends on the geometry, the theoretical model, and the physical parameters.[1] We start our simulations with η_i=2.9.

$R_0/L_n=3.0$ and $T_e/T_i=1$ on the $q_{\min}$ surface. Other parameters are $a/R_0=1/3$ and $r_w=0.28$.

A. Linear eigenmode structures

In the linear phase of the simulations, because $\delta f/f_0 \ll 1$, the nonlinear terms in the equations governing the system can be neglected. The linear theory is then an eigenvalue problem and linear eigenmodes will form in an initial-value simulation. Each eigenmode's amplitude grows exponentially. Such eigenmodes are observed in our simulations and discussed below.

1. Mode gap structure in $q_{\min}$ region

Simulations with various $q_{\min}$ values have been performed to test the sensitivity of the mode structure on the low-order rational number. We notice that when $q_{\min}$ is an integer, the eigenmode structure shows a large gap in the $q_{\min}$ region. A poloidal cross section displaying such a structure with $q_{\min}=1$ is shown in Fig. 1(a1). When $q_{\min}$ deviates from an integer, even if the deviation is very small, e.g., $q_{\min}=0.9552$ or 0.888, the gap disappears. Poloidal cross sections of these two cases are shown in Fig. 1(a2) and Fig. 1(a3), respectively. The device size is $a/\rho_i=250$ in these simulations. For $q_{\min}=2$, we do not see the gap structure until η_i is reduced from 2.9 to 1.3. This indicates that the gap structure may not show up under a strong temperature gradient drive.

2. Mode rational surface distribution

The electrostatic potential can be expressed as a summation of different n (toroidal) and m (poloidal) harmonics:

$$\phi(r,\theta,\zeta)=\sum_n \sum_m \hat{\phi}_{n,m}(r)e^{i(n\zeta-m\theta)}. \tag{12}$$

Due to the symmetry in the ζ direction and the asymmetry in the θ direction, the n harmonics are decoupled in the linear theory and become different eigenmodes. On the other hand, the m harmonics are coupled for each n eigenmode. A mode rational surface for a (n,m) harmonic is located at the radial position r where

$$nq(r)=m. \tag{13}$$

Since q has a minimum value, for each n number, there exists a minimum m which has at least one rational surface and can be expressed as:

$$m_{\min}(n)=\lceil nq_{\min} \rceil, \tag{14}$$

where $\lceil \cdots \rceil$ is the ceiling function defined as $\lceil x \rceil = \min\{k \in \mathbb{Z} | k \geq x\}$.

The rational surface distributions in these simulations are investigated for the formation of the mode gap structures. Among all the n and m harmonics, only the most unstable ones matter. The harmonics up to $n,m=192$ are kept in the simulations here. By analyzing the poloidal (m) spectrum on the $q_{\min}$ surface in our simulations and using an ITG mode property $k_\parallel \approx 0$, which indicates $nq \approx m$, the most unstable harmonics are in the range of $n \in [25,95]$. The rational surface distribution in various simulations is plotted in the column (b) of Fig. 1 (the vertical color lines below the $\langle \phi^2 \rangle$ profile plots). The black lines are the $m=m_{\min}$ rational surfaces, the red lines are the $m=m_{\min}+1$ surfaces, the blues are the $m=m_{\min}+2$ surfaces, and so forth. The $m \geq m_{\min}+8$ surfaces are far away from the $q_{\min}$ region and are thus ignored. We can see that two large rational surface gaps in the $q_{\min}$ region appear due to the degeneration of $m=m_{\min}$ surfaces in the $q_{\min}=1$ cases, while the noninteger $q_{\min}$ cases do not have large gaps (filled up by split $m=m_{\min}$ surfaces).

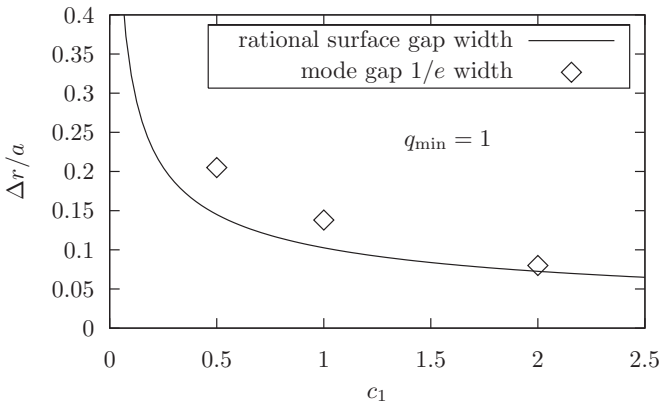

FIG. 2. The width of the ITG potential gaps and the rational surface gaps vs the q-profile curvature c_1.

The simulation results above show that the global mode structure is sensitive to the rational surface distribution. These results can be explained by the toroidal coupling. Normally, the rational surfaces distribute densely all over the radial space. The toroidal coupling makes the global mode structure smooth across the $q_{\min}$ region. When $q_{\min}$ is an integer, the $m=m_{\min}(n)$ rational surfaces degenerate at the $q_{\min}$ position, forming two gaps in which there is no mode rational surface. Inside the gap, only the slab branch of the ITG instability can exist, which is usually much weaker than the toroidal branch. Therefore, the potential intensity is greatly reduced in this region, showing a gap in the global mode structure.

3. Radial width of the mode gaps

The radial width of the mode gaps is sensitive to the q-profile curvature c_1. The $\langle \phi^2 \rangle$ structures and rational surface distribution computed using various c_1 values are shown in Fig. 1(b1-1), Fig. 1(b1), and Fig. 1(b1-2). Here, ϕ is normalized by e/T_e. It can be seen that as the parameter c_1 increases, the widths of the potential gap and the rational surface gap decrease. For an integer $q_{\min}$, from Eqs. (11) and (13), we can derive the width of the rational surface gap for a single n harmonic:

$$\frac{\Delta r}{a}=\sqrt{\frac{1}{nc_1}}. \tag{15}$$

With all the most unstable harmonics considered, the gap width is

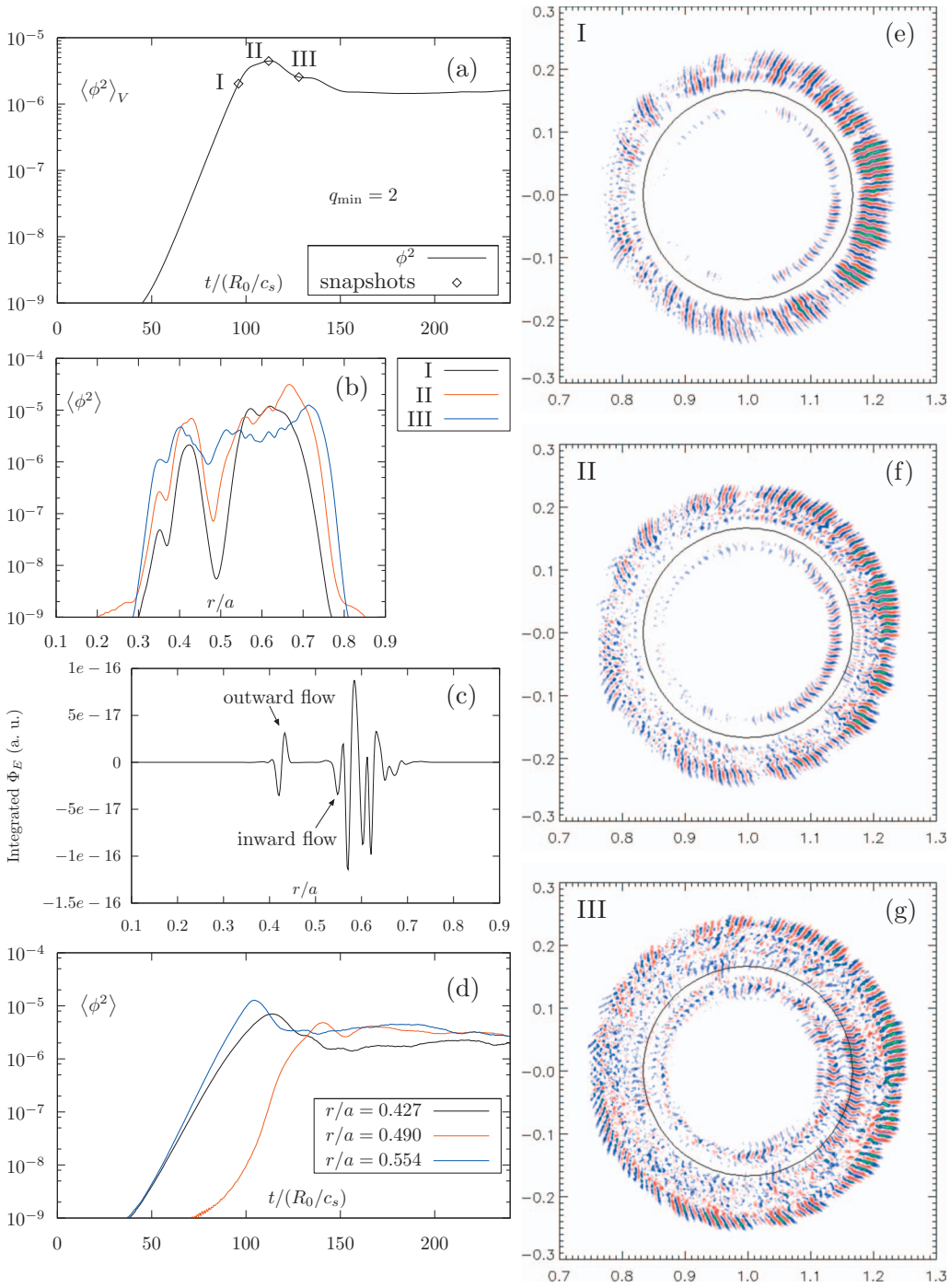

FIG. 3. (Color) ITG mode gap filled up by turbulence. (a) The time history of $\langle\phi^2\rangle_V$ with three snapshots in the early nonlinear phase. (b) The $\langle\phi^2\rangle$ radial profile snapshots. (c) The flux of $\boldsymbol{E}$-field intensity Φ_E integrated from time 96 to 112 (R_0/c_s). (d) The time history of $\langle\phi^2\rangle$ at various positions. (e)-(g) The ϕ poloidal snapshots. Zonal potential is excluded in all plots.

$$\frac{\Delta r_{\min}}{a} = \sqrt{\frac{1}{n_{\max} c_1}}, \tag{16}$$

where $n_{\max}$ is the maximum n number among the most unstable harmonics. In these simulations, $n_{\max}$=95. We define the width of the potential gap to be its $1/e$ width in the $\langle\phi^2\rangle$ profile, indicated by the blue double arrows in the column (b) of Fig. 1. Figure 2 shows the widths of the potential gap and the rational surface gap versus c_1. We can see that the potential gap has a similar width as the rational surface gap, which agrees with the explanation in Sec. III A 2.

B. Nonlinear evolution

As the mode amplitude grows, nonlinear effects become important and the mode eventually saturates. We focus on the $q_{\min}$=2, η_i=1.3, a/ρ_i=500 case to analyze the nonlinear evolution of the ITG turbulence.

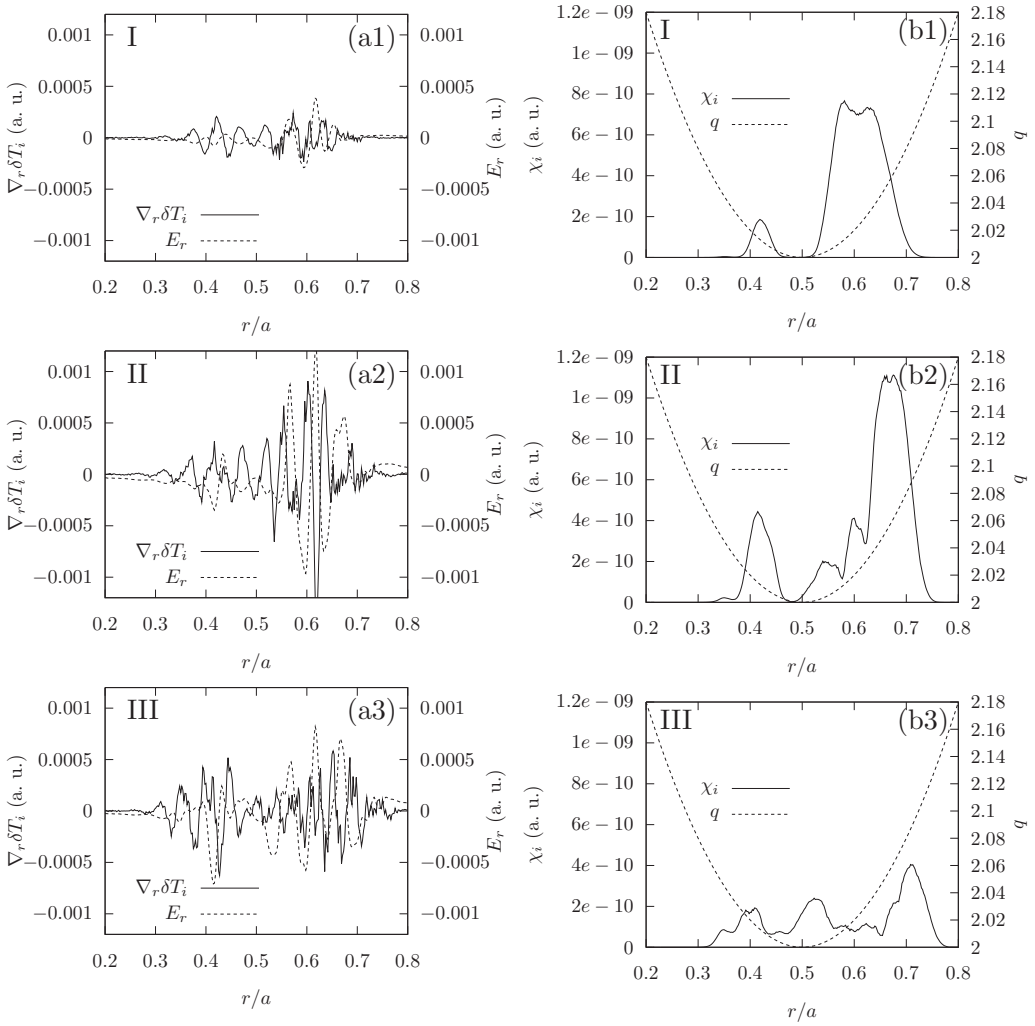

FIG. 4. Perturbed ITG ($\nabla_r \delta T_i$), zonal electric field (E_r), and ion heat conductivity (χ_i) radial profiles of the ITG turbulence snapshots.

1. Gap filled up by turbulence

Figure 3(a) shows the time history of the volume-averaged potential intensity $\langle \phi^2 \rangle_V$ excluding zonal potential. Starting from the time 96 (unit: R_0/c_s), nonlinear effects come into play and the ITG instability saturates. Three snapshots are taken at times 96, 112, and 128. The radial profiles of flux-surface-averaged potential intensity $\langle \phi^2 \rangle$ excluding zonal potential at these time shots are shown in Fig. 3(b). It is seen that the potential gap structure that forms in the linear phase is filled up, which can also be seen from the poloidal cross sections in Figs. 3(e)–3(g). To see how the field energy transfers in the radial direction, we calculate the flux of the $\boldsymbol{E}$-field intensity averaging over the flux surface, which is defined as

$$\Phi_E(r) \equiv \langle E^2 v_{Er} \rangle. \tag{17}$$

Here $E^2 \equiv |\nabla \phi|^2$, and v_{Er} is the radial component of the $\boldsymbol{E} \times \boldsymbol{B}$ drift velocity. For simplicity, the averaging is calculated over the ions on the flux surface. Figure 3(c) shows the time integrated Φ_E in the early nonlinear phase. Two flows going into the $q_{\min}$ region are identified and marked in the figure, implying turbulence spreading is a likely reason for the mode gap being filled up. Figure 3(d) shows the time evolution of $\langle \phi^2 \rangle$ at multiple radial positions. The $r/a = 0.427$ and 0.554 locations are the places where the net flow is zero ($\boldsymbol{E}$-field intensity flows from these points inward and outward simultaneously). The $r/a = 0.490$ location is the place where $\langle \phi^2 \rangle$ gets a minimum value in snapshot I. In the late linear phase, the growth rates of $\langle \phi^2 \rangle$ at $r/a = 0.427$ and 0.554 decrease while the one at $r/a = 0.490$ increases, which confirms that the field energy flows into the $q_{\min}$ region and fills up the potential gap.

2. Fluctuations and structures near $q_{\min}$

Various quantities during saturation are investigated to study the turbulence structures near the $q_{\min}$ surface. We focus on the three snapshots in the early nonlinear stage mentioned above. The perturbed temperature gradient $\nabla_r \delta T_i$, where $\delta T_i \equiv \langle \int (1/2) m v^2 \delta f_i d^3 v \rangle$, the zonal electric field $E_r \equiv -\nabla_r \langle \phi \rangle$, and the ion heat conductivity $\chi_i \equiv \langle \int v_{Er} (1/2) m v^2 \delta f d^3 v \rangle / |\nabla T_i|$ in the snapshots are shown in

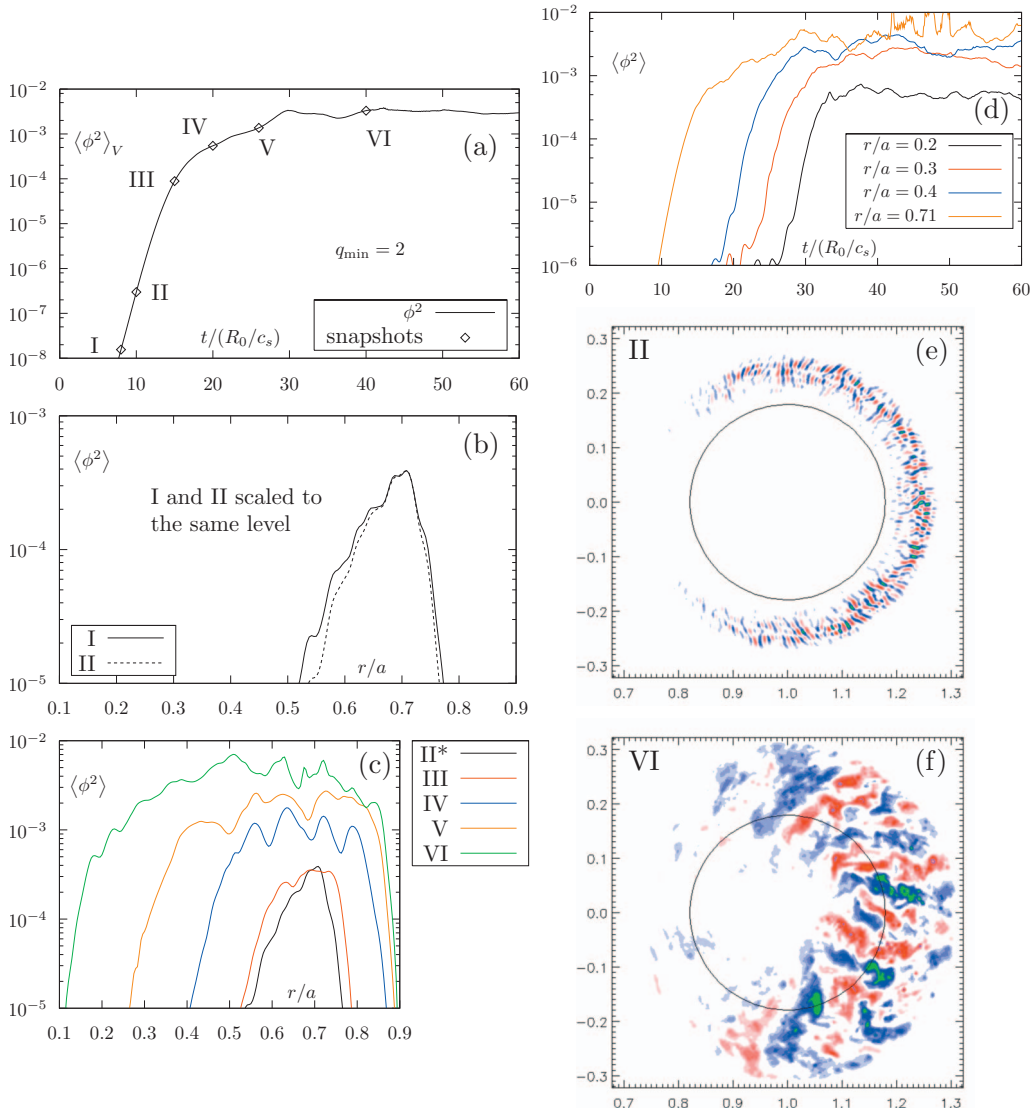

FIG. 5. (Color) Mode structures of the CTEM turbulence. (a) The time history of $\langle\phi^2\rangle_V$. Six snapshots are taken. (b) $\langle\phi^2\rangle$ radial profiles of the first two snapshots scaled to the same level showing the linear eigenmode. (c) Evolution of the $\langle\phi^2\rangle$ in the nonlinear phase. (II*: scaled up) (d) The time history of the $\langle\phi^2\rangle$ at various radial positions. (e) The ϕ poloidal structure of the linear eigenmode. (f) The ϕ poloidal structure in the late nonlinear phase. Zonal potential is excluded in all plots.

Fig. 4. The amplitudes of the perturbed temperature gradient and the zonal radial electric field increase a little as time goes, but they are at a similar level over the radial space. Note that the perturbed temperature gradient and the zonal electric field are antiphase.[34] In the $q_{\min}$ region, no peak or gap was seen. The evolution of the ion heat conductivity profile is similar to the $\langle\phi^2\rangle$ profile. There is a gap near the $q_{\min}$ surface in the linear phase. It is gradually filled up in the nonlinear phase. After saturation, all quantities we studied have similar amplitudes all over the radial domain, with no clear structure seen in the $q_{\min}$ region. Therefore, no profile corrugations are observed in our global simulations.

IV. CTEM TURBULENCE

Magnetic mirrors are made in the bad curvature region of the torus by the spiral shape of the magnetic field lines and the nonuniformity of the field in the poloidal direction. Charged particles can be trapped in these mirrors and drift in the toroidal direction. Such toroidal precession can resonate with the electron drift wave and drive an instability called the CTEM instability.[1] The mode amplitude grows exponentially under the instability drive until nonlinear effects take place and saturate the mode, which then becomes the CTEM turbulence.

A fluid-kinetic hybrid electron model[32,33] is utilized to simulate the CTEM turbulence.[35] We focus on a $q_{\min}=2$, $c_1=2$ case. Parameters on the $q_{\min}$ surface are $R_0/L_n=2.2$ and $T_e/T_i=1$. Other parameters are $r_w=0.32$, $a/R_0=0.358$, and $a/\rho_i=125$. The ITG mode is suppressed by setting $\eta_i=1$. The CTEM instability is excited with $\eta_e=3.1$.

A. Linear eigenmode

Similar to the ITG instability, the CTEM instability also has an eigenmode in the linear stage. Figure 5(a) shows the time history of the volume-averaged fluctuation intensity $\langle\phi^2\rangle_V$. Six snapshots are taken. The radial profiles of the $\langle\phi^2\rangle$

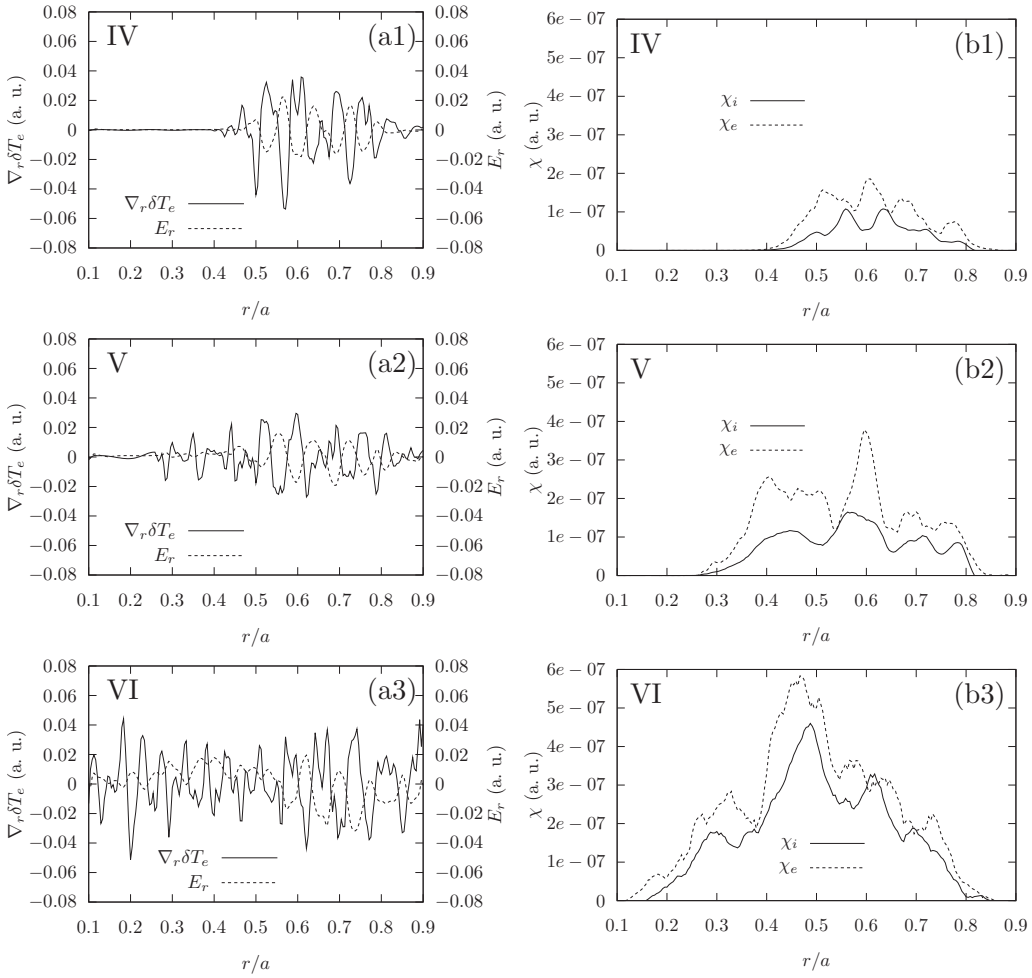

FIG. 6. Perturbed electron temperature gradient ($\nabla_r \delta T_e$), zonal electric field (E_r), and heat conductivity (χ_e and χ_i) radial profiles in the nonlinear snapshots of the CTEM turbulence.

at snapshots I and II, which are both in the linear phase, are scaled to the same level and shown in Fig. 5(b). They have roughly the same shape, indicating an eigenmode is formed. Note that there is no turbulence spreading in the linear phase. The ϕ contour plot at snapshot II is presented in Fig. 5(e), showing the eigenmode's poloidal structure. We can see that the mode grows only in the positive-shear region ($r/a > 0.5$). The negative-shear region is stabilized. This is probably due to the precessional drift reversal of the trapped electrons in the negative magnetic shear.

B. Nonlinear turbulence spreading

In the nonlinear phase, the turbulence is observed to spread not only outward toward the boundary but also inward into the negative-shear side ($r/a < 0.5$). Figure 5(c) shows the $\langle \phi^2 \rangle$ radial profiles of the snapshots taken. The snapshot II profile is scaled up so that the profile shape evolution is clearly seen. From this figure or the ϕ poloidal structure of snapshot VI in Fig. 5(f), we can see that there is no special structure in the $q_{\min}$ region after saturation. The turbulence spreading into the negative-shear region can also be seen in Fig. 5(d), which gives the time history of flux-surface-averaged potential intensity $\langle \phi^2 \rangle$ at various radial locations. The mode at inner locations is stable at first. After saturation in the positive-shear region ($r/a = 0.71$ in this figure), the fluctuation intensities $\langle \phi^2 \rangle$ at $r/a = 0.4$, 0.3, and 0.2 start to grow one by one as turbulence propagates in. We define the turbulence arriving time at a certain flux surface as the time when $\langle \phi^2 \rangle$ at that flux surface passes 10^{-4}. The arriving times at $r/a = 0.2$, 0.3, and 0.4 are 30.6, 26.4, and 22.1 (unit: R_0/c_s), respectively. Considering that $a/R_0 = 0.358$ and the time unit is R_0/c_s, doing a linear fit gives the turbulence spreading speed $v_{ts} = 8.4 \times 10^{-3} c_s$. Notice that electron diamagnetic drift speed is $v_{*e} = \rho_s c_s / L_{T_e}$. In our case $T_e = T_i$, so $\rho_s = \rho_i$. Note that $a/\rho_i = 125$ and $R_0/L_{T_e} = 6.9$, then we can write the turbulence spreading speed in terms of electron's diamagnetic drift speed: $v_{ts} = 0.43 v_{*e}$. This is close to various theoretical estimates.[36,37]

The structures of the perturbed temperature gradient, the zonal electric field, and the heat conductivity profiles after saturation are shown in Fig. 6. We can see that all these quantities spread along with the turbulence into the negative-shear region, leaving no significant structure around the $q_{\min}$ surface.

V. SUMMARY AND CONCLUSIONS

Electrostatic drift wave turbulence in tokamak plasmas with reversed magnetic shear is studied using global gyrokinetic particle simulations. The linear eigenmode of the ITG instability exhibits a mode gap around the minimum safety factor ($q_{\min}$) region, particularly when $q_{\min}$ is an integer, due to the rarefaction of rational surfaces. The CTEM instability is suppressed in the negative-shear region due to the reversal of the toroidal precessional drift of trapped electrons. However, after nonlinear saturation, the ITG gap is filled up by the turbulence spreading and the CTEM fluctuation propagates into the stable negative-shear region. The steady state turbulence occupies the whole volume without any identifiable gap or coherent structures of the heat conductivity, perturbed temperature, or zonal flows in the $q_{\min}$ location or the reversed shear region. Our finding indicates that the electrostatic drift wave turbulence itself does not support either linear or nonlinear mechanism for the formation of internal transport barriers in the reversed magnetic shear when $q_{\min}$ crossing an integer. Other external mechanisms, such as sheared flows generated by MHD activities, are worth pursuing as possible agents to suppress the electrostatic drift wave turbulence and form the internal transport barriers when $q_{\min}$ crossing an integer. Our results of nonlocal effects also raise the issue of the validity of previous local simulations finding the transport reduction due to the precessional drift reversal of trapped electrons or the rarefaction of mode rational surfaces in the reversed shear plasmas.

ACKNOWLEDGMENTS

We acknowledge useful discussions with I. Holod, W. L. Zhang, and Y. Xiao.

This work was supported by the U.S. Department of Energy (DOE) SciDAC GPS-TTBP and GSEP centers. Simulations were performed using supercomputers at NERSC and ORNL.

[1] W. Horton, Rev. Mod. Phys. **71**, 735 (1999).
[2] M. Hugon, B. v. Milligen, P. Smeulders, L. Appel, D. Bartlett, D. Boucher, A. Edwards, L.-G. Eriksson, C. Gowers, T. Hender, G. Huysmans, J. Jacquinot, P. Kupschus, L. Porte, P. Rebut, D. Start, F. Tibone, B. Tubbing, M. Watkins, and W. Zwingmann, Nucl. Fusion **32**, 33 (1992).
[3] F. M. Levinton, M. C. Zarnstorff, S. H. Batha, M. Bell, R. E. Bell, R. V. Budny, C. Bush, Z. Chang, E. Fredrickson, A. Janos, J. Manickam, A. Ramsey, S. A. Sabbagh, G. L. Schmidt, E. J. Synakowski, and G. Taylor, Phys. Rev. Lett. **75**, 4417 (1995).
[4] E. J. Strait, L. L. Lao, M. E. Mauel, B. W. Rice, T. S. Taylor, K. H. Burrell, M. S. Chu, E. A. Lazarus, T. H. Osborne, S. J. Thompson, and A. D. Turnbull, Phys. Rev. Lett. **75**, 4421 (1995).
[5] F. Romanelli and F. Zonca, Phys. Fluids B **5**, 4081 (1993).
[6] X. Garbet, C. Bourdelle, G. T. Hoang, P. Maget, S. Benkadda, P. Beyer, C. Figarella, I. Voitsekovitch, O. Agullo, and N. Bian, Phys. Plasmas **8**, 2793 (2001).
[7] Y. Kishimoto, J.-Y. Kim, W. Horton, T. Tajima, M. LeBrun, S. Dettrick, J. Li, and S. Shirai, Nucl. Fusion **40**, 667 (2000).
[8] N. Miyato, Y. Kishimoto, and J. Li, Nucl. Fusion **47**, 929 (2007).
[9] C. J. McDevitt and P. H. Diamond, Phys. Plasmas **14**, 112306 (2007).
[10] R. E. Waltz, M. E. Austin, K. H. Burrell, and J. Candy, Phys. Plasmas **13**, 052301 (2006).
[11] Y. Idomura, S. Tokuda, and Y. Kishimoto, Nucl. Fusion **43**, 234 (2003).
[12] M. Yagi, T. Ueda, S.-I. Itoh, M. Azumi, K. Itoh, P. H. Diamond, and T. S. Hahm, Plasma Phys. Controlled Fusion **48**, A409 (2006).
[13] B. B. Kadomtsev and O. P. Pogutse, in *Reviews of Plasma Physics*, edited by M. A. Leontovitch (Consultants Bureau, New York, 1970), Vol. 5, pp. 249–400.
[14] M. A. Beer, G. W. Hammett, G. Rewoldt, E. J. Synakowski, M. C. Zarnstorff, and W. Dorland, Phys. Plasmas **4**, 1792 (1997).
[15] Y. Koide, M. Kikuchi, M. Mori, S. Tsuji, S. Ishida, N. Asakura, Y. Kamada, T. Nishitani, Y. Kawano, T. Hatae, T. Fujita, T. Fukuda, A. Sakasai, T. Kondoh, R. Yoshino, and Y. Neyatani, Phys. Rev. Lett. **72**, 3662 (1994).
[16] C. Greenfield, C. Rettig, G. Staebler, B. Stallard, M. Austin, K. Burrell, J. DeBoo, J. deGrassie, E. Doyle, P. Gohil, R. Groebner, J. Lohr, G. McKee, W. Peebles, C. Petty, R. Pinsker, B. Rice, T. Rhodes, E. Synakowski, R. Waltz, and L. Zeng, Nucl. Fusion **39**, 1723 (1999).
[17] E. Joffrin, G. Gorini, C. D. Challis, N. C. Hawkes, T. C. Hender, D. F. Howell, P. Maget, P. Mantica, D. Mazon, S. E. Sharapov, G. Tresset, and E.-J. Workprogramme, Plasma Phys. Controlled Fusion **44**, 1739 (2002).
[18] D. Frigione, L. Garzotti, C. D. Challis, M. D. Baar, P. D. Vries, M. Brix, X. Garbet, N. Hawkes, A. Thyagaraja, L. Zabeo, and J. E. Contributors, Nucl. Fusion **47**, 74 (2007).
[19] S. Gunter, A. Gude, J. Hobirk, M. Maraschek, S. Saarelma, S. Schade, R. Wolf, and A. U. Team, Nucl. Fusion **41**, 1283 (2001).
[20] A. Thyagaraja, P. J. Knight, and N. Loureiro, Eur. J. Mech. B/Fluids **23**, 475 (2004).
[21] J. Q. Dong, Z. Z. Mou, Y. X. Long, and S. M. Mahajan, Phys. Plasmas **11**, 5673 (2004).
[22] Z. Lin, T. S. Hahm, W. W. Lee, W. M. Tang, and R. B. White, Science **281**, 1835 (1998).
[23] Z. Lin and T. S. Hahm, Phys. Plasmas **11**, 3 (2004).
[24] T. S. Hahm, P. H. Diamond, Z. Lin, K. Itoh, and S.-I. Itoh, Plasma Phys. Controlled Fusion **46**, A323 (2004).
[25] X. Garbet, L. Laurent, A. Samain, and J. Chinardet, Nucl. Fusion **34**, 963 (1994).
[26] T. S. Hahm, Phys. Fluids **31**, 2670 (1988).
[27] A. J. Brizard and T. S. Hahm, Rev. Mod. Phys. **79**, 421 (2007).
[28] W. Lee, J. Comput. Phys. **72**, 243 (1987).
[29] Z. Lin and W. W. Lee, Phys. Rev. E **52**, 5646 (1995).
[30] I. Holod and Z. Lin, Phys. Plasmas **14**, 032306 (2007).
[31] W. Zhang, Z. Lin, and L. Chen, Phys. Rev. Lett. **101**, 095001 (2008).
[32] Z. Lin and L. Chen, Phys. Plasmas **8**, 1447 (2001).
[33] Z. Lin, Y. Nishimura, Y. Xiao, I. Holod, W. L. Zhang, and L. Chen, Plasma Phys. Controlled Fusion **49**, B163 (2007).
[34] S. E. Parker, C. Kim, and Y. Chen, Phys. Plasmas **6**, 1709 (1999).
[35] Y. Xiao and Z. Lin, Phys. Rev. Lett. **103**, 085004 (2009).
[36] O. D. Gurcan, P. H. Diamond, T. S. Hahm, and Z. Lin, Phys. Plasmas **12**, 032303 (2005).
[37] Z. Guo, L. Chen, and F. Zonca, Phys. Rev. Lett. **103**, 055002 (2009).